Secular Evolution in Late-Type Spiral Galaxies

A Senior Honors Thesis

Presented in Partial Fulfillment of the Requirements for graduation *with research distinction* in Astronomy in the undergraduate colleges of The Ohio State University

by

Man-Hong Wong

The Ohio State University
June 2010

Project Adviser: Professor Paul Martini, Department of Astronomy

Secular Evolution in Late-Type Spiral Galaxies

Man-Hong Wong

Department of Astronomy, The Ohio State University, 140 West 18th Avenue, Columbus, OH 43210, wong.316@osu.edu

ABSTRACT

Galaxy evolution through internal rather than external processes is known as secular evolution. Evidence for secular evolution comes in various forms, most notably the development of a pseudobulge. Pseudobulges differ from merger-built bulges because they exhibit disk-like features. While the bulges of most spirals are best-fit by a Sérsic surface brightness profile with index $n = 4$ (also known as a de Vaucouleurs $r^{1/4}$ profile), pseudobulges typically have $n = 1 - 3$, where an $n = 1$ Sérsic profile corresponds to a second exponential profile (in addition to the disk itself). We used the exponential surface brightness profile of pseudobulges to identify these components in our sample of 20 late-type spiral galaxies. Late-type disks are well-suited to study signs of secular evolution because any past interactions and mergers would have developed at least a small bulge and changed their classification. There is evidence that more massive disk galaxies may be more likely to drive mass inwards and produce a pseudobulge. We perform decompositions of the galaxies to find these features. We also study the the concentrations of polycyclic aromatic hydrocarbons (PAHs) as a function of mass because they have been shown to trace molecular gas, which is the fuel needed to form the stars that make up a pseudobulge. NGC2805, a lower-mass galaxy, was the only galaxy in our sample that has a pseudobulge. We also found no correlation between the central concentration of PAH emission and the mass. This implies that more massive galaxies are not more efficient at driving gas inwards.

1. Introduction

Galaxies can evolve through both external and internal processes. At early times, dissipative collapse (Eggen et al. 1962, Sandage 1990) and mergers (Toomre 1977a) were the dominate mechanisms for galactic evolution. These violent processes, in particular mergers, induce dissipation in the disk, causing the formation of bulges and elliptical galaxies (Kormendy & Kennicutt 2004). As the Universe expands, mergers become less frequent, giving

way to internally driven processes, known as secular evolution. Secular evolution involves interactions between stars or gas clouds with larger scale structures such as bars, spiral arms, and dark matter halos. These processes will dominate the Universe in the distant future, but some galaxies already show signs that they have evolved in this manner.

One indicator that a galaxy has undergone secular evolution is the presence of a pseudobulge. Pseudobulges, like classical bulges, are high concentrations of central stellar mass. To create the stars that make up a pseudobulge, gas needs to be driven inwards, which can happen through a variety of processes. Theory, observations, and simulations have shown that bars, ovals, and global spiral structures redistribute gas in galaxies. All of these structures produce a dense, central concentration of gas that collapses to form stars (Kormendy & Kennicutt 2004, Schmidt 1959). The results are pseudobulges.

Pseudobulges are distinguishable from classical bulges because they exhibit disk-like properties. Classical bulges are dynamically hot, and relatively featureless, resembling elliptical galaxies (Fisher & Drory 2008). These types of bulges are typically modeled with the well-known de Vaucouleurs $r^{1/4}$ profile (de Vaucouleurs 1948), which also fits well to the luminosity profiles of elliptical galaxies. Pseudobulges, on the other hand, retain properties of the disk as it is formed. These features include: kinematics dominated by rotation (Kormendy 1993); flattening similar to that of their outer disk (Fathi & Peletier 2003, Kormendy 1993); mid-IR colors similar to those of the outer disk (Fisher 2006); nuclear bars (Erwin & Sparke 2002); nuclear rings and/or nuclear spirals (Carollo et al. 1997); and exponential surface brightness profiles (Andredakis & Sanders 1994, Fisher & Drory 2008). This study uses the exponential surface brightness profiles of pseudobulges for identification.

An exponential surface brightness profile has a Sérsic index $n = 1$. The Sérsic profile (Sérsic 1968) is a generalization of the de Vaucouleurs law which allows the exponent in the de Vaucouleurs profile to be a free parameter. This light profile is commonly expressed as an intensity profile:

$$I(R) = I_e e^{-K[(R/R_e)^{1/n}-1]}, \tag{1}$$

where R_e is the radius that encompasses half of the total flux, I_e is the intensity at R_e, n is the Sérsic index, and $K(n)$ is chosen so that R_e is the effective radius. The de Vaucouleurs profile has a Sérsic index $n = 4$. This means that the exponential profile is less centrally concentrated and falls off quickly at large radii compared to the de Vaucouleurs profile (Gra-

ham & Driver 2005). Andredakis & Sanders (1994) show that many late-type spirals are better described by two exponential profiles than an inner $r^{1/4}$ and an outer exponential.

We choose to study secular evolution in late-type spiral galaxies, in particular those classified as Sd in the Hubble sequence. There have been numerous studies of early and intermediate-type disk galaxies (Andredakis & Sanders 1994, Carollo et al. 1997, 1998, Carollo & Stiavelli 1998, Carollo 1999, Seigar et al. 2002, Courteau et al. 1996), but there are far fewer studies on later-type spirals. Pure disk galaxies are the best candidates to be dominated by secular evolution because any past interations and mergers would have created at least a small bulge and changed their classification. Bulges detected in these galaxies are most likely a result of secular evolution and are classified as pseudobulges.

Our hypothesis is that more massive galaxies have a higher probability to form a pseudobulge. A comprehensive survey of edge-on, bulgeless disks by Dalcanton et al (2004) found strong dust lanes in galaxies with circular velocities $v_c > 120$ km s^{-1} (corresponding to a mass of 10^{10} M$_\odot$; Bell & de Jong 2001). However, more slowly rotating galaxies showed no dust lanes. Their interpretation is that gravitational instabilities are balanced by interstellar medium (ISM) turbulence in lower-mass galaxies, which produces a more diffuse, extended dust distribution. Gravitational instabilities dominate over turbulence in more massive galaxies to create their narrow dust lanes. If turbulence can prevent the cold ISM from gravitational collapse, star formation, and mass inflow, then pseudobulges will not form. We therefore expect to find a lower fraction of pseudobulges in low-mass galaxies.

PAH emission is an excellent tracer of the molecular gas needed to make pseudobulges. PAHs are large molecules associated with dust stochastically heated by high-energy photons and dominate the 8 μm bandpass of the Infrared Array Camera (IRAC; Allamandola et al. 1989, Fazio et al. 2004). PAH emission correlates well with mm CO emission, which is an excellent tracer of the cold ISM (Regan et al. 2006). We can study the central concentration of PAH emission as a function of mass to determine if more massive galaxies are more efficient at driving gas inwards. We can also confirm if the low-mass galaxies completely lack cold gas and dust with the PAH maps, rather than that the gas and dust have a more extended vertical distribution. A deficiency in gas and dust in the lower-mass sample means secular evolution is inhibited in these galaxies.

The outline of this thesis is as follows. In §2 we describe the data and the steps we took to process it. We explain how we analyzed the data using the program GALFIT in §2. In

§4 we provide the results of our analysis. In §5 we discuss our results and the implications they may have towards secular evolution. We summarize our conclusions in §6.

2. Sample and Processing

The sample consists of 20 late-type disk galaxies, eleven low-mass and nine high-mass. The properties of the galaxies are listed in Table 1. To group the galaxies according to their mass, we used the same classification as Dalcanton et al. (2004); galaxies with $V_c < 120$ km s^{-1} are considered low-mass galaxies. All the observations used in this study were taken by the *Spitzer Space Telescope* using the IRAC instrument. This instrument produces images in four infrared bandpasses that are centered at 3.6, 4.5, 5.8, and 8 μm. We used the IRAC 3.6 μm and 4.5 μm images to measure the surface brightness profiles of each galaxy because these two wavelengths avoid dust extinction commonly found in bluer bandpasses and the emission in these bandpasses is dominated by starlight. We used the 8 μm images to study PAH emission.

There were times when it was necessary to use other observations of the galaxies to determine some properties. To accurately determine the circular velocity of the galaxies, HI observations were obtained with the *Very Large Array*. Nuclear star clusters, found in approximately 75% of late-type galaxies (Böker et al. 2002, 2004), were located with *Hubble Space Telescope* images. The *Hubble Space Telescope* has excellent resolution, so these images were used to determine if the galaxies contain nuclear star clusters and bars.

The data taken by the *Spitzer Space Telescope* were downloaded using the software *Leopard*. Of the 20 galaxies, 15 required new observations and the remaining 5 galaxies coincided with other studies. We chose to download the Basic Calibrated Data (BCD) files instead of the raw data because the basic processing of the data done by Spitzer is sufficient for our study. For the most part, only the IRAC channel 1 (3.6 μm) and IRAC channel 4 (8 μm) images were used in this study; however, for UGC1862, the CH1 image was not centered on the galaxy, so we used the CH2 (4.5 μm) image to measure the surface brightness profile.

The *Spitzer Space Telescope* BCD files still require further processing before they are suitable for analysis. We used a process known as artifact mitigation to correct effects due

to the array technology. The code, written by Sean Carey[1], was used on the raw data to correct the following effects: Muxbleed, Column Pulldown/Pullup, Electronic Banding, and First Frame Effect. Muxbleed is the saturation of a pixel to the point where data counts spill over to other pixels in the same row. This occurs when the signal of a very bright pixel, corresponding to an object such as a bright star, overwhelms the CCD detector with starlight. Column pulldown/pullup occurs under similar circumstances as muxbleed, but only effects channels 1 and 2. When very bright sources hit the detector, the intensities of the pixels above and below the position of the bright source are shifted, creating a vertical streak. Electronic banding is a bias shift in a row that contains a bright source and is seen only in channels 3 (5.8 μm) and 4. Finally, the first frame effect, which can be seen in all channels, arises because changes in the settings such as frame time and Fowler number in-between observations will affect the overall bias of each array. The artifact mitigation code works to some extent at correcting these problems; however, it is not perfect. For example, muxbleed is still present in UGC6446 because of a bright star in the field of view.

After artifact mitigation, the data were processed further with MOPEX (MOasicker and Point source EXtractor), a package developed at the *Spitzer Space Center*. We utilized two features of MOPEX: background matching for the individual frames and creation of a mosaic from the BCD files. MOPEX can be run either from the command line or using the Graphical User Interface. The latter of the two methods offered all of the necessary options we required to process the BCD frames, so we used this method in our analysis.

MOPEX has a variety of pipelines that are used to process BCD files, of which we used the overlap pipeline and the mosaic pipeline. The former performs background matching between overlapping frames and the latter combines the individual BCD images into a mosaic. Before we ran the files through the pipelines, we matched the dimensions of the four images in order to make the PAH images. To do this, we used an overlap pipeline with only the Fiducial Image Frame module. The products of the mosaic pipeline are the images used during the analysis of the galaxies.

The overlap pipeline is necessary to process the images of the galaxies because it brings the background of the individual BCD files to a common level. This is necessary because the analysis algorithm we used calculates the background noise, which means variations in this level will produce invalid results. We used input data files, uncertainty images, and mask

[1]The code can be found at this site: http://spider.ipac.caltech.edu/staff/carey/irac_artifacts/

images as the inputs to the pipeline. Of the available modules of this pipeline, we implemented MedFilter, Detect, Mosaic Interpolate, Compute Overlap Correction, and Quicklook Mosaic. The MedFilter module subtracts the background for the data images to prepare for the Detect module, the Detect module produces maps that flag the pixels of bright objects that should not contribute to the background matching, and the Mosaic Interpolate module projects the input data images onto a 2-D plane. MOPEX interpolates the input pixel values to the output array of pixels. There are four options for interpolation; we chose to use the drizzle method. This is the preferred method when more than 10 BCD frames are used to create the mosaic. The Compute Overlap Correction module computes the correction needed to bring the background level of all the images to a constant value. Finally, the Quicklook Mosaic module produces a mosaic to check if the overlap correction was successful. This pipeline produces corrected BCD images that are used by the mosaic pipeline.

The main purpose of the mosaic pipeline is to create a mosaic of the BCD files, and MOPEX provides many options for doing this. We used the same inputs as we did in the overlap pipeline, but with the corrected image files. The mosaic pipeline performs interpolation of the BCD images and allows the user to choose from four different schemes to produce the final mosaic, of which we once again chose the drizzle scheme. In the interpolation step, MOPEX projects the input images onto a 2-D plane and corrects for optical distortions. In the drizzle scheme, the input pixels are shrunk by a factor specified by the user and then projected onto the output image frame. During the analysis of the galaxies, we used the mosaic images and the coverage maps produced by this pipeline.

3. Analysis

The main focus of this project is to determine whether the presence of secular evolution in late-type spiral galaxies has any relationship with the mass of the galaxy. To determine whether a galaxy has undergone secular evolution, we analyzed the images created by the MOPEX pipelines. This analysis employed two pieces of information that we extracted from the IRAC mosaics: a map of the stellar mass density and a map of the cold ISM. We used the 3.6 μm mosaics as the maps of the stellar mass density (except for UGC1862). We created PAH images from the channel 1 and 4 mosaics to produce a map of the cold ISM. We used these maps to search for evidence of secular evolution in the form of pseudobulges and enhanced PAH emission.

3.1. PAH Images

We mapped the cold, dusty ISM by creating PAH emission images using the IRAC data. The results of Regan et al. (2006) show that the distributions of CO and PAH are nearly identical in their sample. We used PAH images to map the dust distribution in the galaxies. Excess PAH emission would indicate an excess in gas and dust, which would lead to a higher star formation rate and possibly a pseudobulge. Mapping the cold ISM also allowed us to check if the results of Dalcanton et al. (2004) apply to the galaxies in our sample, because PAH emission is an excellent tracer of dust. If there is a higher concentration of gas and dust towards the center of the galaxies, this could mean mass is being pushed into the central regions. We used the CH4 mosaics to map the PAH emission and study the distribution of gas and dust.

The 8 μm data are dominated by PAH emission, but stellar flux is still present. Because the CH1 mosaics map the stellar emission, these images were used to subtract the stellar flux from the CH4 mosaics. Helou et al. (2004) extrapolated 3.6 μm data to longer wavelengths to find that a scaling factor of 0.232 had to be multiplied to this bandpass to correctly subtract the stellar flux. Before we removed the stellar emission from the CH4 data, we subtracted the sky level from both channels so we could obtain accurate radial profiles. We also performed a cross-convolution with the mosaics and PSFs, created by TinyTim (Krist & Hook 1999) to correct for the fact that the diffraction limit will be larger in the CH4 data. We subtracted the CH1 data from the CH4 data pixel by pixel to yield PAH images after we applied the scaling factor and made the two modifications to the mosaics. The final PAH images are displayed in Figure 1.

3.2. Ellipse Task

The ellipse task, contained in IRAF (Image Reduction and Analysis Facility), employs an iterative method described by Jedrzejewski (1987) to fit multiple isophotes to a galaxy, varying the length of the semi-major axis for each iteration. An isophote is a curve that connects points with equal light intensities. CH1, and CH2 for UGC1862, mosaics are the best choices as the inputs because almost all of the emission comes from stellar sources and dust extinction is small. The first elliptical isophote is generated using the center, ellipticity, and position angle supplied by the user. The length of the semi-major axis for this isophote can be adjusted to any value; however, we used the default value of 20 pixels for each trial. Giving an accurate center for the galaxy greatly increases the likelihood of a valid

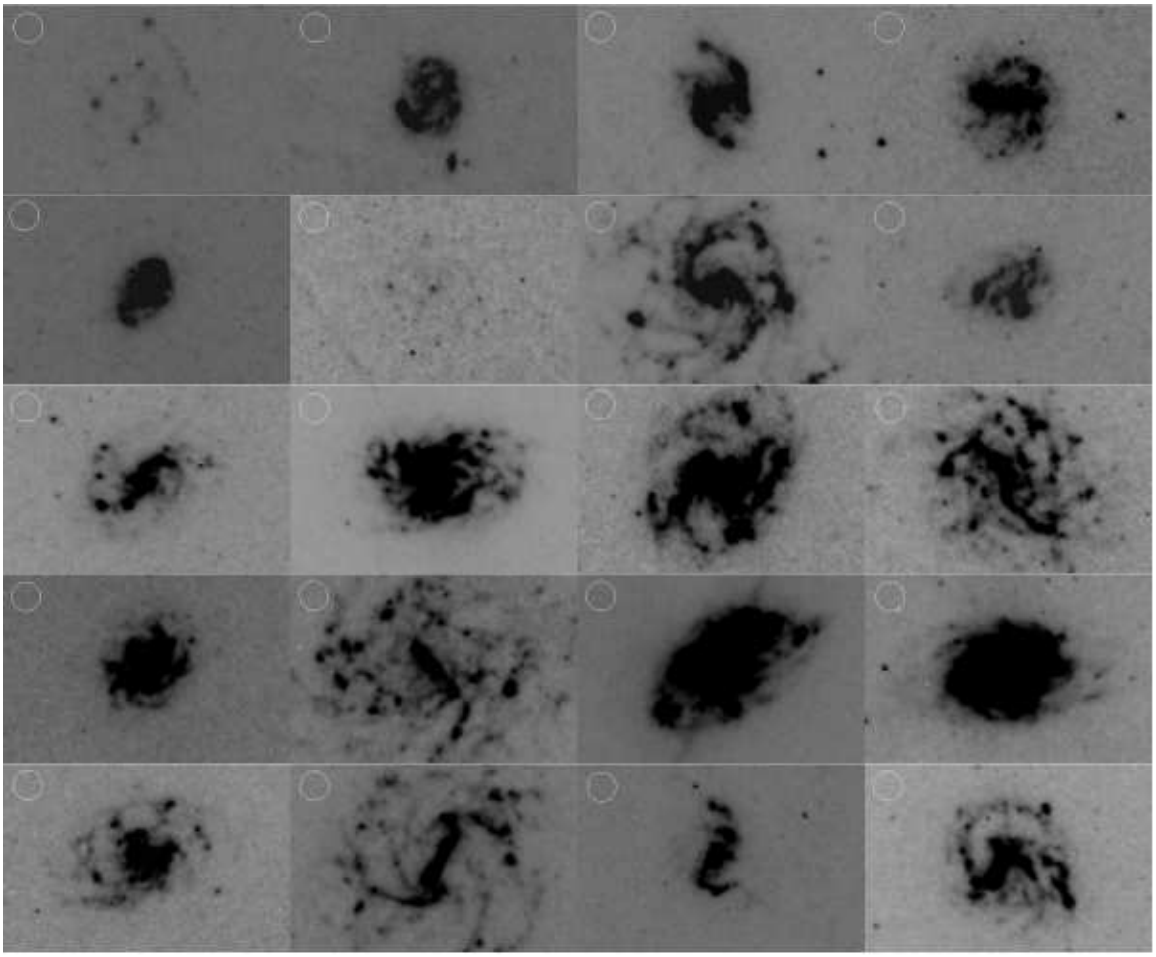

Fig. 1.— PAH images for the galaxies in our sample. From left to right, top to bottom: ESO501-G023, UGC1862, NGC4561, NGC3906, ESO418-G008, UGC6446, NGC2805, ESO544-G030, NGC3794, NGC4713, NGC4519, UGC6930, NGC4942, PGC3853, NGC0337, NGC6509, PGC6667, NGC5964, IC1291, and ESO555-G027. We measured the PAH flux within a 21"-diameter circle centered on the galaxy center (see Table 2, column 6). The size of this aperture is showen in the upper left corner of each image. North is up and East is to the left in these images.

fit because the program can mistake bright stellar objects as the target galaxy. We used the pixel with the highest flux for the location of the center of the galaxy. Much like the initial semi-major axis, the initial ellipticity and position angle can be set to their default values, 0.1 and 30, respectively, because the algorithm can accurately determine the correct values for these parameters. The task increases the semi-major axis length of the isophote after it determines the best elliptical isophote for that length, which is done by performing a least-squares fit. The algorithm repeats the process with an increased semi-major axis length for each iteration until the specified maximum semi-major axis length is reached.

One other important input to the ellipse task is a Bad Pixel Mask, which flags areas of the input image that should not be considered during the fitting process. We used the program SExtractor (Bertin & Arnouts, 1996) to create the Bad Pixel Masks for each galaxy. The masks are important because the CH1 mosaics contain many stellar objects that are unassociated with the galaxy and affect the analysis of the mosaics. We also flagged areas that were imaged less than four times because the signal to noise ratio of these pixels is not as high. These areas were determined by using the coverage map produced by MOPEX.

The output is a series of best-fit elliptical isophotes as a function of semi-major axis. At each semi-major axis length, the best-fit isophote is defined by the mean isophotal intensity, ellipticity, and position angle (see Figure 2). We found the isophotes that encompass all of the flux and averaged their parameters. The average values of the largest isophotes provide the best estimate of the inclination and PA of the galaxy because all of the galaxy is considered in the fit. These values were used as the initial parameters in the GALFIT analysis.

We also used the ellipse task to measure the flux of the PAH emission in a circle with a 10.5" radius. Because PAH emission is an excellent tracer of molecular gas, a high density of PAH molecules would indicate an abundance of gas, which would inevitably form into stars. We chose to measure the flux in the central regions because our hypothesis is that gas is driven towards the center by gravitational instabilities. We used a 21"-diameter aperture because observations of the CO distributions from the *IRAM* 30m telescope have this aperture size. A higher concentration of PAH flux in the more massive galaxies would show that the gravitational instabilities do push gas inwards. The results of this analysis are displayed in Table 2.

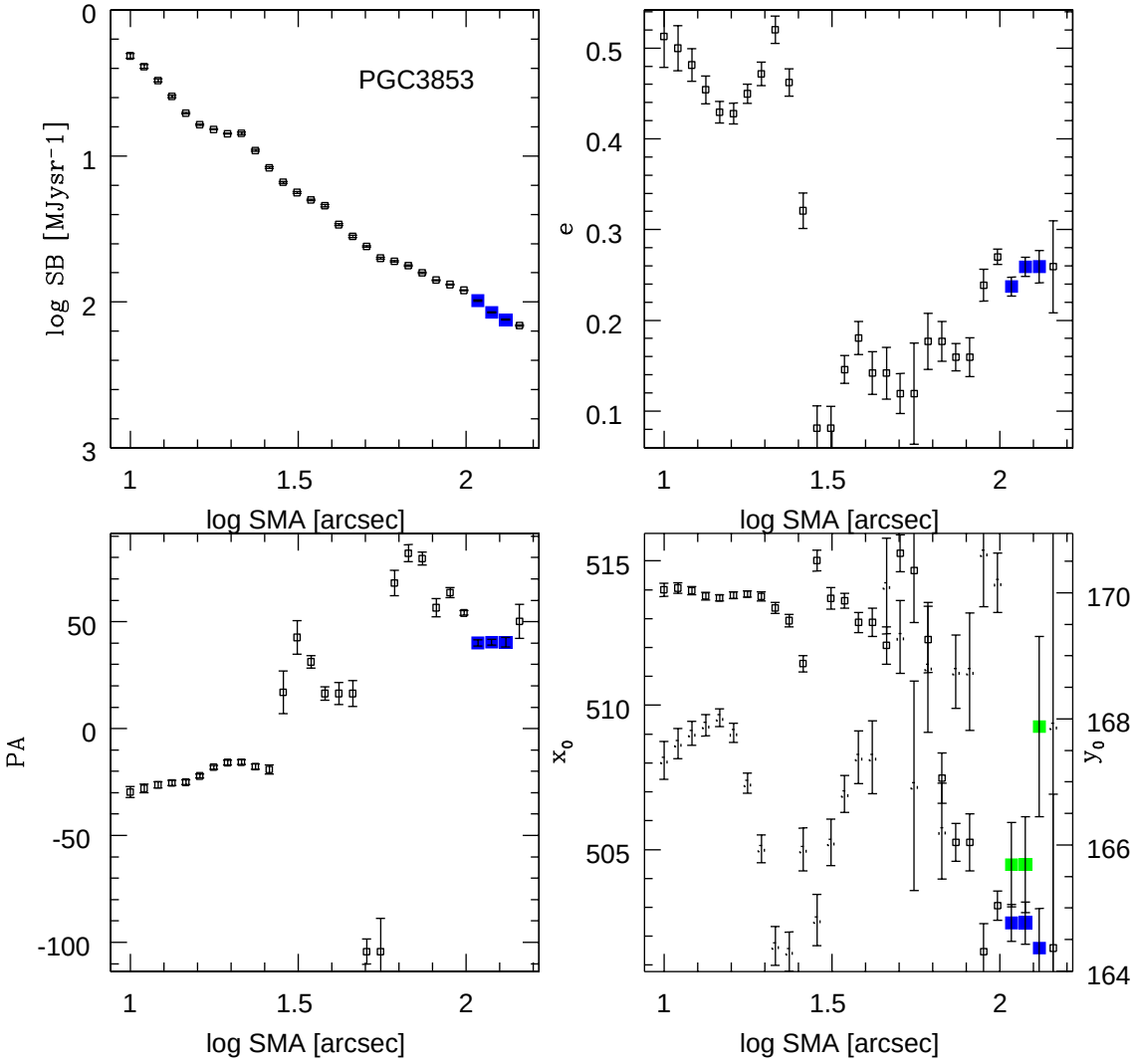

Fig. 2.— An example of an output of the ellipse task for PGC3853. The colored points indicate the values we averaged together to determine the initial parameters for the GALFIT analysis.

3.3. GALFIT

GALFIT is a two-dimensional image decomposition program designed to fit light profiles to galaxies with an arbitrary number of functions to allow for maximum flexibility (Peng et al. 2002). Using images from the *HST*, GALFIT is capable of fitting components such as disks, bulges, bars, and even spiral arms; however, the resolution of images obtained by the *SST* are not as sharp as *HST* images, so more complicated components like spiral arms were very difficult to fit. We used GALFIT to identify the structural components of each galaxy because, as Häussler et al. (2007) explain, the algorithm excels in fitting multiple components in a consistent and reliable manner, limited only by the amount of computer memory and speed.

GALFIT accepts four images as the inputs for each fit: an image of the galaxy, a noise array (sigma image), a point-spread function (PSF), and a dust (or bad pixel) mask. The algorithm requires an image of the galaxy, but the others are optional. We opted to include all of the inputs except a noise array because this image is generated by GALFIT when one is not supplied. GALFIT generates the noise array by using the parameters in the header of the BCD files. We used the same mask as the one created for the ellipse task. The other inputs are discussed in more detail below.

We modified the 3.6 μm bandpass mosaics in order to comply with the requirements of GALFIT. The images generated by MOPEX have units of MJy/sr, but GALFIT requires them to be in Data Numbers (DN) or electrons (these units are related by the gain). Using *IRAF*, we converted the units of the images from MJy/sr to DN by using constants provided in the header of the BCD files.

As an option, GALFIT can convolve the model images with a PSF. All the images in our sample carry an imprint of the observing setup, caused by imperfections or diffractions in the telescope optics. This process is optional, but it helps in accurately fitting the light profile. We used TinyTim (Krist & Hook 1999) to create the PSF. The convolution is done using a fast Fourier transform method to reduce the computational time. By using a PSF, we could use the PSF function to fit stars in the input images.

The dust image is also optional but helps GALFIT determine what sources contribute to the galaxy when the field is crowded. The dust image will flag stars that should be ignored when the model is created. Without this input, GALFIT will occasionally interpret stars

unassociated with the galaxy as part of it, leading to a model that does not accurately fit the light profile of the galaxy. We found that using the dust image helped GALFIT determine the correct center, which resulted in better fits.

One of the strengths of GALFIT is how little the algorithm relies on the initial parameters provided by the user. GALFIT requires an input file that lists the functions, with initial parameters, used during the fit. The creator of GALFIT stresses how the algorithm is able to return a good fit ($\chi^2_\nu \approx 1-2$) even with poor choices for initial input parameters ($\chi^2_\nu \approx 10^5 - 10^7$). We force GALFIT to use the averaged parameters from the ellipse task as the initial parameters to insure the algorithm fits the correct object, but allowed the remaining parameters to float. We found that GALFIT returns better results when the initial estimates for the parameters are visually consistent with the image, specifically the axis ratio and position angle.

Following a procedure described by Weinzirl et al. (2009), a two or three stage fitting process was used to decompose the galaxy into a disk, bar, and bulge. The first stage involved fitting a Sérsic model to the galactic disk. The center, position angle, and axis ratio of the galaxies were taken from the results of the ellipse task and held fixed. By visually examining the HST images, we determined whether there is evidence of a bar in the galaxies. If a bar is present, the second stage fit the disk of the galaxy with an exponential profile and the bar with a Sérsic profile. The exponential light profile has a Sérsic index $n = 1$. For the Sérsic models, GALFIT determines the index. The initial parameters of the bar fit were determined by visually examining the input image. If a bar was not found by examining the HST images or residuals of the first stage fits, we fit the galaxy with an exponential disk and PSF for a nuclear star cluster, if applicable. The final stage added another Sérsic component to allow for the presence of a pseudobulge. We set the initial Sérsic index for the pseudobulge to one, as that is the most likely value for late-type disk galaxies, but allowed it to vary.

The outputs of GALFIT are the original image, model, residual image, and a log file with the fit parameters (see Figure 3-6 and Table 2). We used the residual image and the value of the reduced chi squared, χ^2_ν, to determine the quality of the fit. To determine the best model of the galaxy, GALFIT minimizes χ^2_ν:

$$\chi^2_\nu = \frac{1}{N_{dof}} \sum_{x=1}^{nx} \sum_{y=1}^{ny} \frac{(flux_{x,y} - model_{x,y})^2}{\sigma^2_{x,y}} \tag{2}$$

where N_{dof} is the number of degree of freedom in the model, flux and model are the intensity values of a given x, y pixel position of the input image and computed model, respectively, and $\sigma^2_{x,y}$ is the Poisson error at each pixel. The stage with the lowest value of χ^2_ν and proper parameters for the components was deemed the best model for that galaxy.

We do not expect all the galaxies in our sample to contain a pseudobulge, but we tried to fit all the galaxies with this component. If stellar flux remains in the residuals of the disk and bar fits (near the center of the galaxy), we directed the final Sérsic component to fit this starlight. In some cases, the best fit values for the bulge component were clearly unphysical and therefore we rejected them. For example, sometimes the fit converged to Sersic index $>$ 1000, which was likely due to PSF uncertainties or small-scale structure around a nuclear star cluster. In other cases, GALFIT crashed because it tried to fit the galaxies with more components than necessary, which was a clear sign that the galaxy did not contain a pseudobulge.

Although we obtained models for all the galaxies in our sample, there were various problems we encountered when using GALFIT. When given an input image with high resolution like the images from HST, GALFIT is able to fit many of the subtle structures such as spiral arms; however, with the lower resolution IRAC images, only simpler structures, such as the galaxy disk and bar, were fit. Occasionally, the algorithm had difficulty differentiating between the disk of the galaxy and the spiral arms, which led to poor fits and higher values of χ^2_ν. Examples of this can be seen in the residuals of NGC0337 and IC1291, which have strong spiral structure (see Figures 5 and 6, respectively).

Another problem we encountered was the presence of nuclear star clusters. GALFIT has the capablility to fit PSFs, but specifying the location of the PSF is very important because the algorithm may fail if the initial and final positions are not well matched. We determined the location of the nuclear star clusters in the HST images and fixed the PSF fit to the corresponding pixels in the input image. In most cases, this helped reduce the χ^2_ν and produced less residual structure.

As GALFIT minimizes χ^2_ν, there is a chance that the algorithm will get lost in a local minimum. This will result in a low χ^2_ν, but not the best model. To prevent this, we inspected each fit to make sure that GALFIT located the correct objects. We also examined the model and residual for each fit and compared them to the previous fits. When GALFIT returned

a result with unrealistic values, we fixed the parameters of the disk and bar components so GALFIT could focus on the bulge fit. We had to keep in mind that not all of the galaxies contain pseudobulges; so if the bulge component continually returned bad fits, we concluded that the galaxy did not contain a pseudobulge.

4. Results

The primary objective of this study was to determine if there is a correlation between the mass of a galaxy and evidence of secular evolution in the form of a pseudobulge or enhanced PAH emission. Due to the findings of Dalcanton et al. (2004), we predicted that higher-mass galaxies have a higher probability of developing a pseudobulge because gravitational instabilities dominate these galaxies. This would cause stellar mass and dust to flow into the center of the galaxy, which would create a pseudobulge at the center of the galaxy. Using GALFIT to decompose the galaxy, we were able to fit the galaxies with disk, bar, and bulge models.

The results of the GALFIT analysis are displayed in Table 2 and the model and residual images are shown in Figures 3-7. The GALFIT results show that only one galaxy, NGC2805, contains a pseudobulge. This galaxy is part of the low-mass sample. As for the other galaxies, GALFIT was not able to produce better results when we added the bulge component. At times, GALFIT produced unrealistic parameters for the models as the algorithm attempted to minimize χ^2_ν. We tried to hold some of the parameters fixed during the fit, but the final value of χ^2_ν was higher than those produced in fits without the bulge model. In other cases, the algorithm crashed because we tried to fit more functions to the image than necessary. We conclude NGC2805 is the only galaxy in our sample with a pseudobulge.

5. Discussion

5.1. Presence of Bars

In the review by Kormendy & Kennicutt (2004) of secular evolution and pseudobulges, they describe how barred galaxies drive gas toward the center of the disks. The inflow is caused by shocks produced when gas interacts with the bar. The excess of gas will inevitably lead to star formation, which would create a pseudobulge. This is not the only way for gas

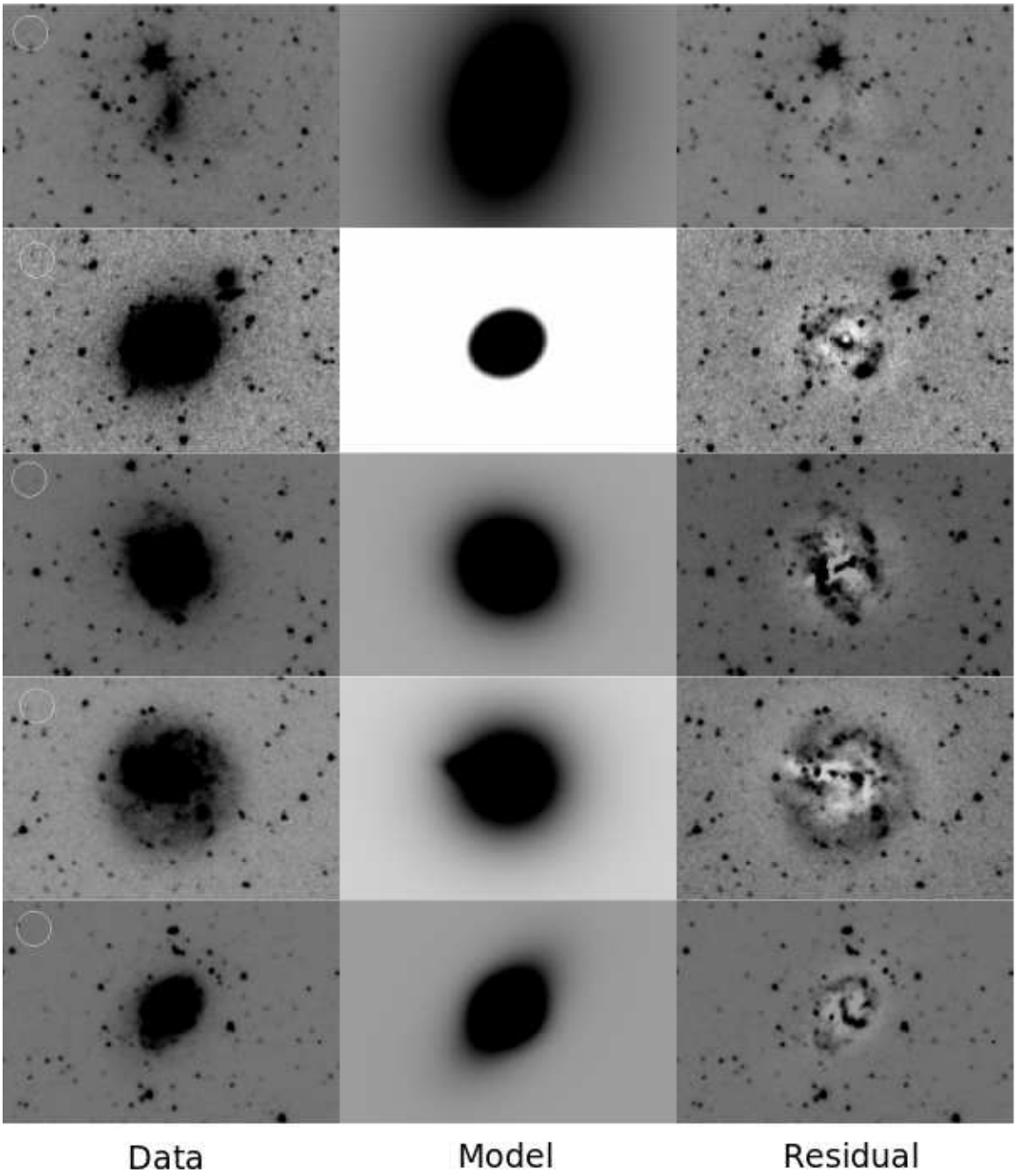

Fig. 3.— 3.6 μm data, GALFIT models, and residuals for ESO501-G023, UGC1862, NGC4561, NGC3906, and ESO418-G008. The parameters for the model are listed in Table 2. A 21" circle is in the upper-left corner of each row. North is up and East is to the left.

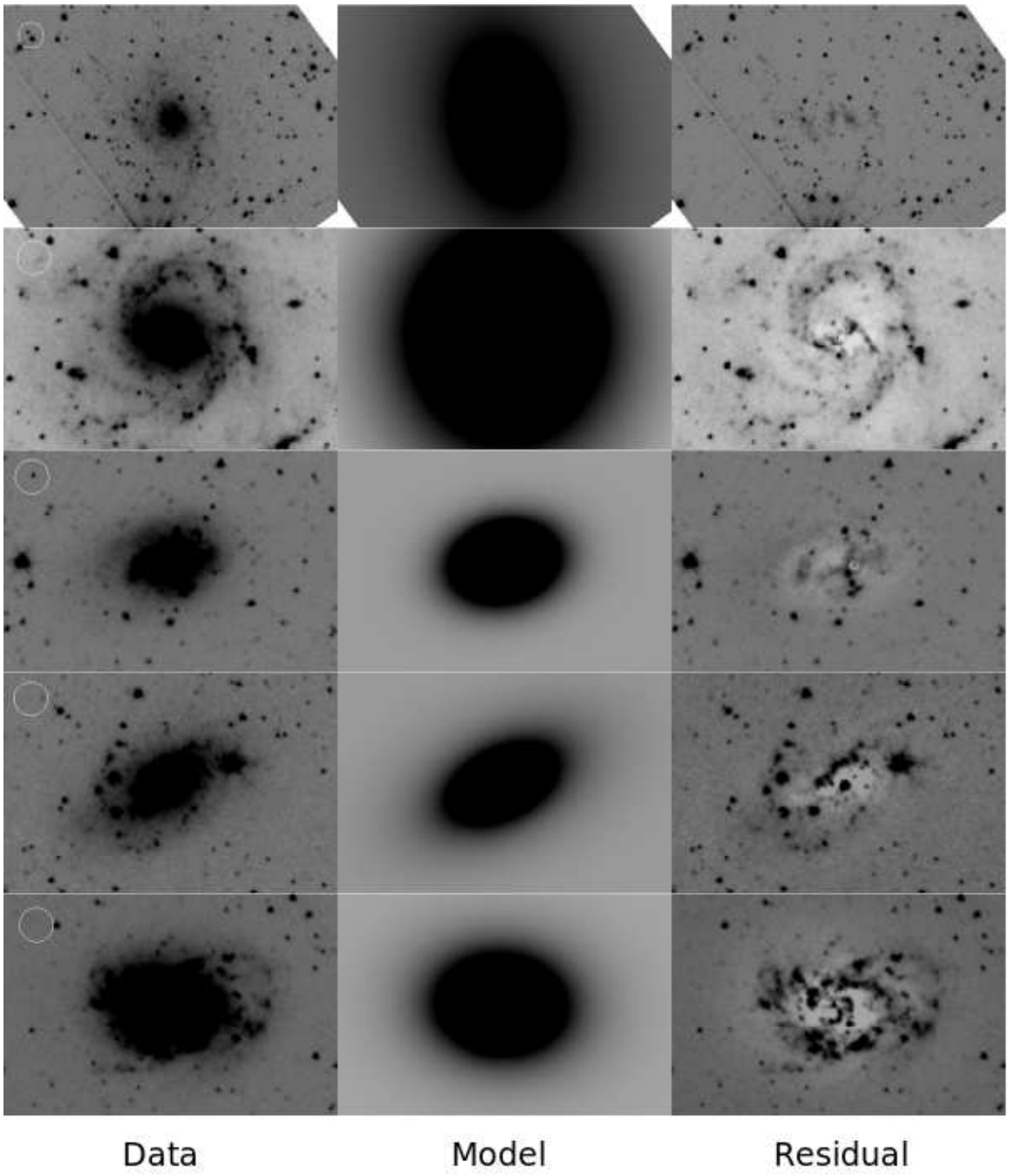

Fig. 4.— Same as Figure 3 for UGC6446, NGC2805, ESO544-G030, NGC3794, and NGC4713.

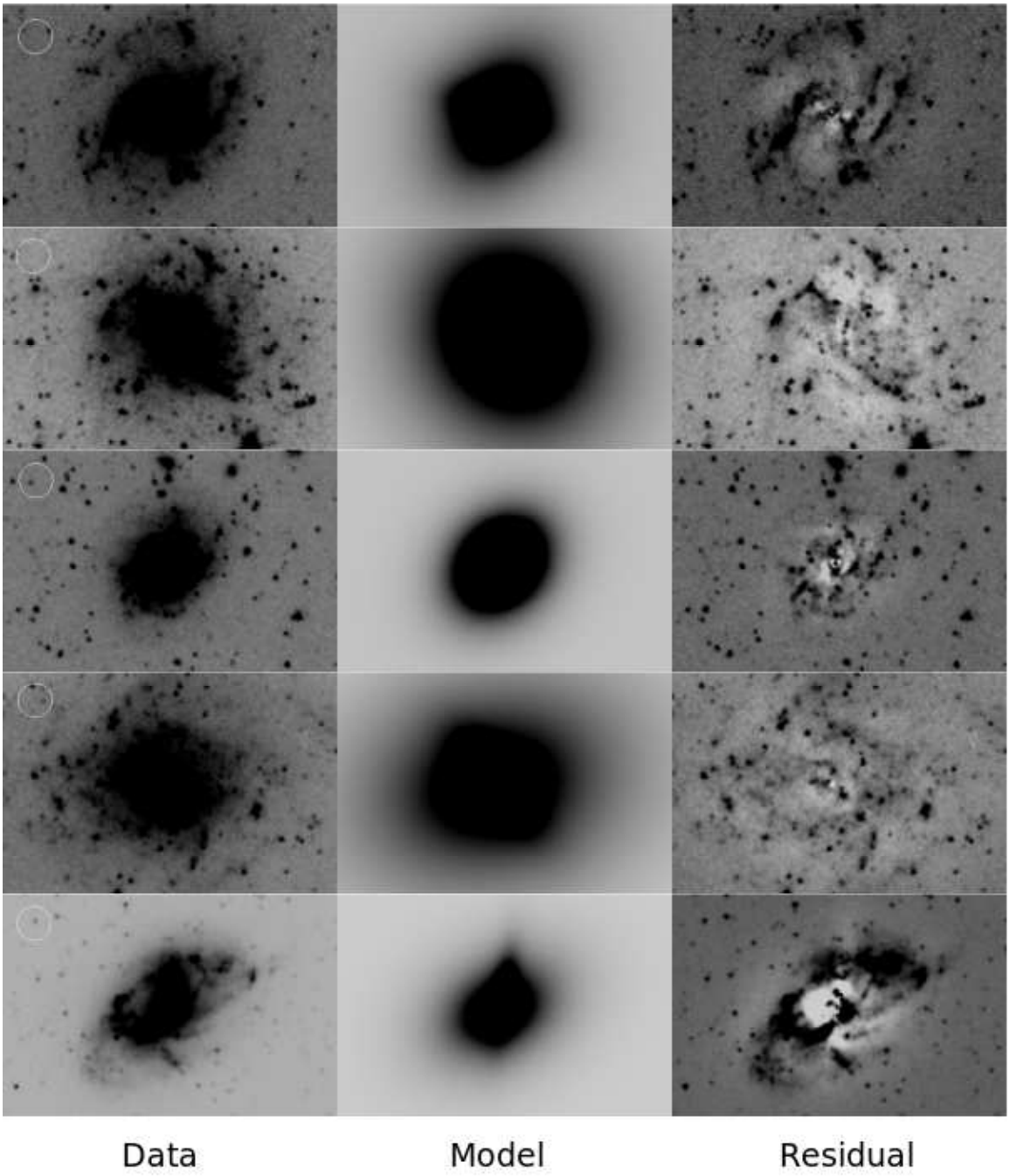

Fig. 5.— Same as Figure 3 for NGC4519, UGC6930, NGC4942, PGC3853, and NGC0337.

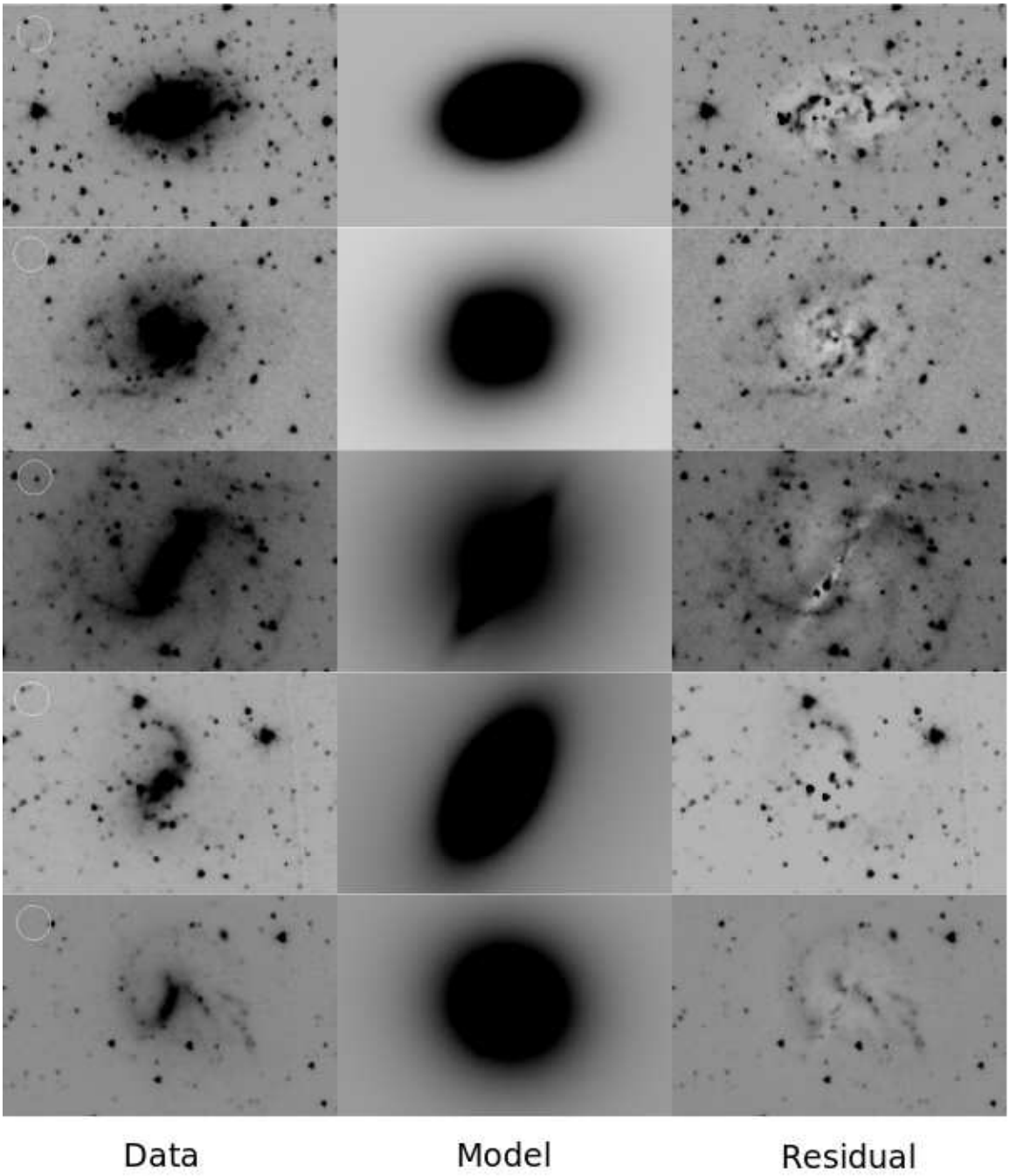

Fig. 6.— Same as Figure 3 for NGC6509, PGC6667, NGC5964, IC1291, and ESO555-G027.

to be driven inwards. In late-type, grand-design spirals, shocks similar to those produced in barred galaxies will also cause an inflow of gas. The only galaxy in our sample with a pseudobulge has strong spiral structure.

Our GALFIT results show bar components in 45% of the lower-mass galaxies and 89% of the more massive sample. Visual examination of the CH1 mosaics found 55% and 67% of lower-mass and higher-mass galaxies, respectively, contain bars. A study done by Nair & Abraham (2010) also found that a larger percentage of more massive galaxies have bars. Approximately 2/3 of late-type spiral galaxies have bars (de Vaucouleurs 1963); 65% of the disks in our sample have these structures.

The fact that such a large percentage of the high-mass galaxies have bars may indicate that they are more likely to develop these structures. Bars are generally believed to form because the orbits of stars in the inner regions of galaxies are changed by gravitational instabilities. This effect will spread outwards over time to create a bar. The observation that bars are more common in the higher-mass sample suggests that they are more prone to these instabilities.

The only galaxy that contains a pseudobulge in our sample is unbarred, but there are some reasons that may explain this. The bars found in late-type spiral galaxies are weaker than those found in early-type disks (Nair & Abraham 2010). This means not as much mass will be driven towards the center of the disk. Also, the excess gas found in those galaxies may have resulted from shocks produced from gas accelerating and decelerating through the spiral arms. NGC2805 shows strong spiral structure that can drive mass inwards. Another reason may be that NGC2805 was once barred but the structure was destroyed as gas was driven inwards (Hasan & Norman 1990). Komendy & Kennicutt (2004) mention that the gas that fueled the star formation could have resulted from bar-driven inflow, even if a bar is not currently present.

5.2. Disk Models

We fit each galaxy with a Sérsic profile function in the first stage of our GALFIT analysis. The disks of spiral galaxies are well fit by an exponential light profile over several disk scale lengths; the Sérsic index is ~ 1 in an exponential light profile (Freeman 1970).

GALFIT determines the Sérsic index when the Sérsic profile is used as a model. The values for this parameter are listed in Table 2 for each fit. There is no clear correlation between the Sérsic index of the disk and the circular velocity of the galaxy (see Figure 7).

5.3. PAH Flux

The PAH images were used to map the gas concentrations in the galaxies. We measured the central concentration of PAH flux in a circle with radius 10.5" and found no clear relationship between the PAH flux and the circular velocity of the galaxy (see Figure 8). Although the more massive galaxies show more PAH emission on average, this does not show there is an excess of molecular gas because the high-mass galaxies will also have more stars, so the ratio of PAH/stellar emission might be the same in the low and high-mass galaxies.

Our results do not show a correlation between the PAH flux and the presence of a bar. In §5.1, we described how bars can drive gas towards the center of the galaxy (Kormendy & Kennicutt 2004). If bars do drive gas inwards, we should find a higher concentration of PAH emission in the barred galaxies. There are a few reasons why we do not see this relationship. Gas can be driven inwards as it passes through the spiral arms. This process has a longer timescale than bar driven processes, but the final results are similar. The bars in late-type spirals are weaker than bars found in early-type spirals (Nair & Abraham 2010). If bars do drive gas towards the center, weaker bars may be less effective at this. Also, bars have been shown to weaken as gas is driven inwards, eventually destroying itself if enough mass flows inward (Hasan & Norman 1990). Some of the unbarred galaxies with an abundance of PAH emission could have been barred at some point. These reasons could explain why we do not see a clear relationship between the PAH flux and the presence of a bar.

5.4. Presence of a Pseudobulge

The results of the GALFIT analysis do not support our hypothesis. Due to the findings of Dalcanton et al. (2004), we expected that higher-mass galaxies had a greater probability of developing a pseudobulge. They attribute the narrow dust lanes found in higher-mass disks to gravitational instabilities dominating the ISM turbulence. This would drive mass towards the center of the galaxy, which eventually creates a pseudobulge. The only galaxy

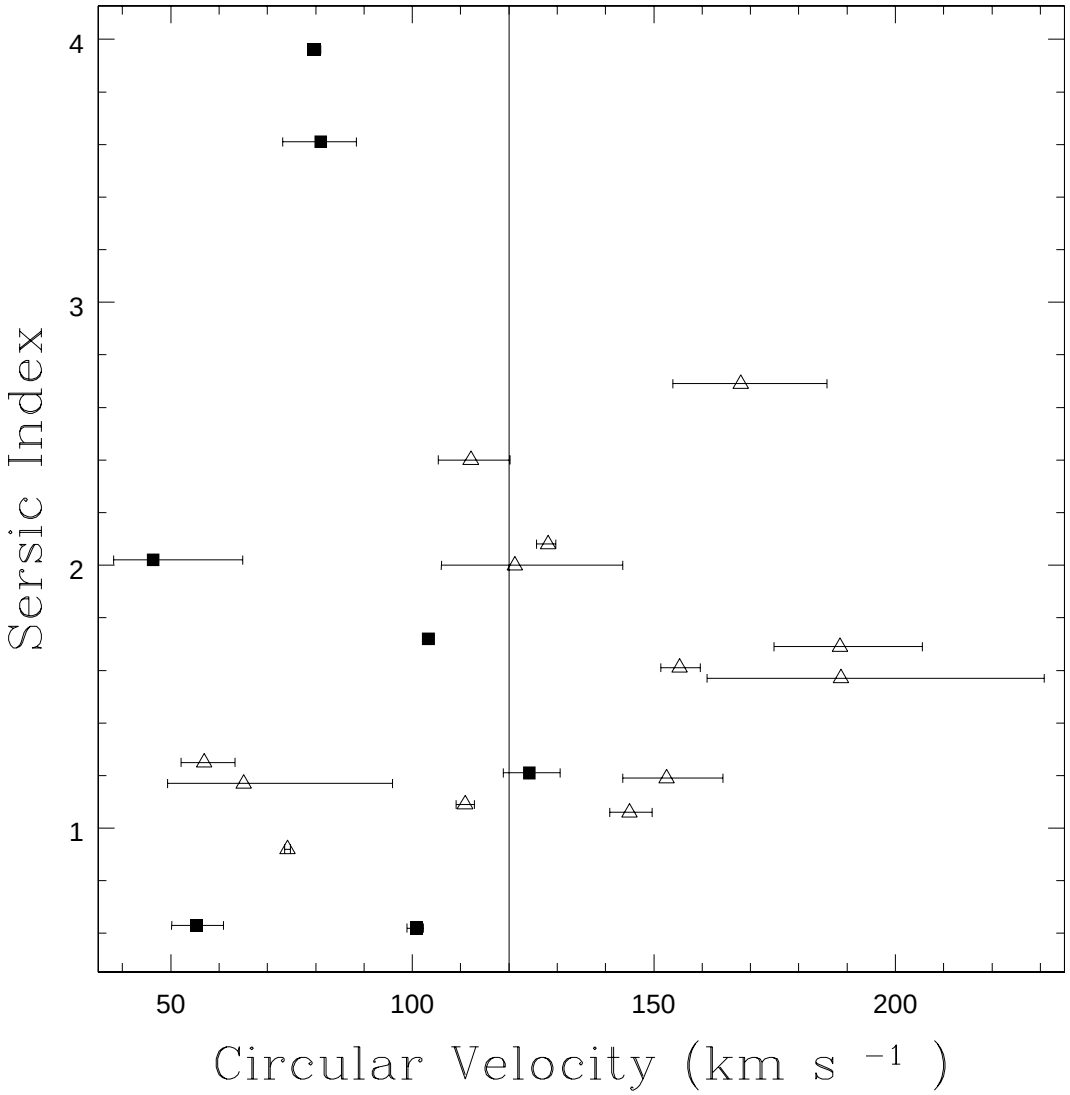

Fig. 7.— Sérsic index n as a function of circular velocity v_c. The filled squares denote unbarred galaxies and the open triangles represent barred galaxies. The vertical line shows the division of low-mass and high-mass galaxies.

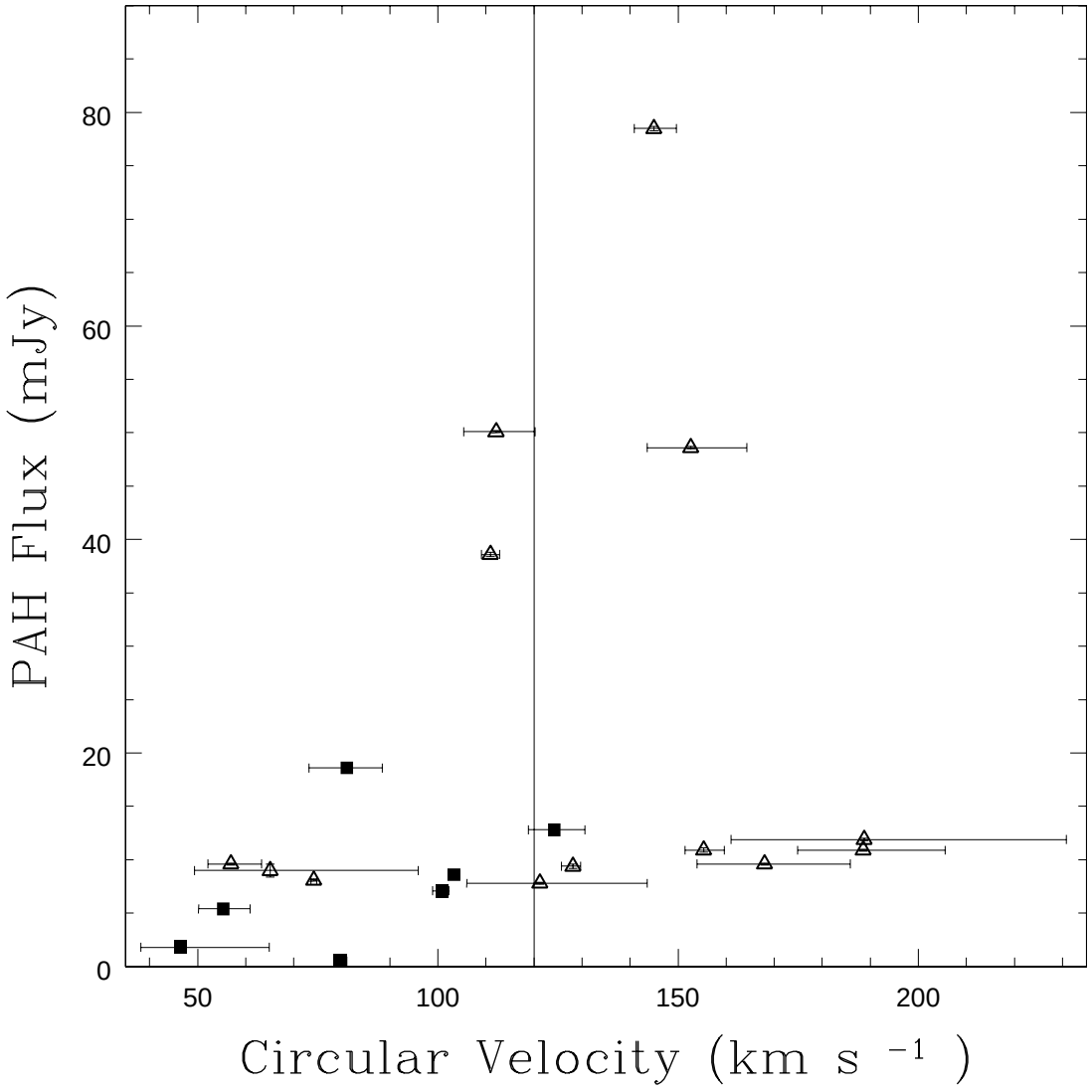

Fig. 8.— PAH flux (Jy) as a function of circular velocity v_c. The fluxes were measured in a circle with a 10.5" radius. The filled squares are the data for the unbarred galaxies and the open triangles represent barred galaxies. The vertical line splits the low-mass and high-mass samples.

in our sample that contains a pseudobulge is a lower-mass disk, which is in conflict with this scenario.

One possible explanation for our results is that the gravitational instabilities do not drive enough mass towards the center to develop a pseudobulge. The processes that produce the narrow dust lanes in more massive galaxies may not lead to a substantial amount of mass inflow. Enough gas needs to be driven inwards to create the stars which would make an excess of stellar light above the disk. The gravitational instabilities may cause mass inflow, but not at the level needed to create pseudobulges.

Another possible explanation is that there is not enough stellar mass in the center of the galaxy for the algorithm to fit a bulge component. Gas and dust could be driven inwards, but not to the extent to create enough stars to form a pseudobulge. Kormendy & Kennicutt (2004) discuss how the distinction between the disk and bulge is subtle. If there is only a slight increase of stellar flux near the center of the galaxy, GALFIT could interpret this as part of the disk. GALFIT will only be able to fit a bulge component if enough stars are formed from the excess gas.

These explanations do not describe why the only bulge found in our sample is in a lower-mass galaxies. Our results clearly demonstrate that galaxy mass does not increase the likelihood that a late-type galaxy will have a pseudobulge. A more comprehensive sample would help to determine whether it was just a coincidence that we did not find any pseudobulges in the higher-mass galaxies. The process of forming a pseudobulge is still an unsolved question. Gravitational instabilities might not be the process that drives the mass that forms a pseudobulge. Another mechanism, which does not have a dependence on mass, may be responsible for the inflow of mass.

6. Conclusions

The main goal of this study was to determine whether secular evolution had any dependence on the mass of the galaxies in late-type spiral disks. Our sample consists of 20 late-type spiral galaxies, classified as Sd galaxies in the Hubble sequence. The late-type disk galaxies are most likely dominated by secular evolution because any past interactions or mergers would have developed a bulge and changed their classification. The galaxies span a

wide range in mass, with 11 galaxies classified as low-mass ($v_c < 120$ km s^{-1}). The sample was observed with the *Spitzer Space Telescope* using the IRAC instrument. IRAC produces images in four bandpasses that are centered at 3.6, 4.5, 5.8, and 8 μm. The 3.6 μm and 4.5 μm observations accurately trace the stellar mass distribution of these galaxies with little dust extinction. The 8 μm mosaics are excellent tracers of PAH emission, and therefore the cold ISM. Using these images, we created maps of the stellar mass density and the cold ISM.

Our motivation comes from a comprehensive survey of edge-on, bulgeless disks by Dalcanton et al. (2004). These authors found strong vertical color gradients in galaxies with circular velocities $v_c > 120$ km s^{-1} (corresponding to a stellar mass of 10^{10} M$_\odot$; Bell & de Jong 2001), while galaxies with lower circular velocities did not show strong vertical color gradients. Their interpretation is that the more massive galaxies have narrow dust lanes, while the dust is more diffuse in the low-mass disks. They associate the lack of narrow dust lanes in the slowly rotating galaxies to a balance between the gravitational instabilities and ISM turbulence. If turbulence can support the cold ISM against gravitational collapse and mass inflow, the formation of bulges will not take place. We hypothesized that a larger fraction of higher-mass galaxies would show signs of secular evolution.

One common indicator that a galaxy has undergone secular evolution is the presence of a pseudobulge. Classical, i.e. merger-built, bulges share many properties with elliptical galaxies, including a de Vaucouleurs $r^{1/4}$ light profile (de Vaucouleurs 1948, Fisher & Drory 2008); pseudobulges, on the other hand, exhibit many disk-like properties which allow us to distinguish between the two types of bulges. The feature we focused on is the exponential surface brightness profile of pseudobulges (Andredakis & Sanders 1994). We used a two-dimensional decomposition algorithm called GALFIT to fit multiple light profiles to the each galaxy. We found one galaxy with a pseudobulge, NGC2805. This galaxy has a circular velocity $v_c = 81.05^{+7.42}_{-7.85}$, so it is considered a lower-mass disk. Our results do not support our hypothesis that more massive galaxies have a higher probability to develop a pseudobulge.

Our results could imply that the processes that produce the narrow dust lanes found in many high-mass galaxies do not lead to a substantial amount of mass inflow. We measured the PAH emission in the central regions of all the galaxies and found no correlation with the circular velocity. Figure 8 shows that there are galaxies in both samples with an abundance of PAH flux and a lack of PAH flux. Because PAH emission is an excellent tracer of molecular gas (Regan et al. 2006), we do not find a correlation between the circular velocity and abundance of molecular gas, which supports our conclusion.

The results of this study show that another mechanism is most likely responsible for the mass inflow that produces a pseudobulge. There is evidence that secular evolution drives mass inwards, but the cause of the inflow is still unknown. As the universe expands, secular processes will become the dominate form of evolution, so determining the mechanisms that drive mass inwards will only become more relevant.

Table 1. Galaxy Parameters

Galaxy	v_{circ} (km s^{-1})	RA (J2000.0)	Dec (J2000.0)	i (deg)	PA (deg)	d (Mpc)	Distance Reference	Bar Classification
(1)	(2)	(3)	(4)	(5)	(6)	(7)	(8)	(9)
ESO501-G023	$46.37^{+18.48}_{-8.16}$	10:35:23	-24:45:15	37	223.6	14.2	1	Yes
UGC1862	$55.34^{+5.53}_{-5.15}$	02:24:24	-02:09:44	43.35	21.65	17.34	2	No
NGC4561	$56.91^{+6.43}_{-4.82}$	12:36:08	+19:19:22	34.25	227.3	12.3	1	Yes
NGC3906	$65.09^{+30.80}_{-15.76}$	11:49:39	+48:25:32	16.46	184.95	16		Yes
ESO418-G008	$74.17^{+0.60}_{-0.56}$	03:31:30	-30:12:48	55.58	317.9	21.02	2	Yes
UGC6446	$79.72^{+1.33}_{-0.79}$	11:26:40	+53:44:48	52.5	189.43	15.54	1,2	No
NGC2805	$81.05^{+7.42}_{-7.85}$	09:20:20	+64:06:11	37.5	299.99	28	1	No
ESO544-G030	$100.88^{+1.42}_{-2.03}$	02:14:56	-20:12:44	48.52	107.56	15.72	2	No
NGC3794	$103.32^{+1.12}_{-1.01}$	11:40:54	+56:12:07	54.81	123.06	24.7	1	No
NGC4713	$110.91^{+1.98}_{-1.84}$	12:49:58	+05:17:41	45.24	273.95	17.53	1,2	Yes
NGC4519	$112.11^{+8.15}_{-6.73}$	12:33:30	+08:39:18	42.42	354.94	29.01	1,2	Yes
UGC6930	$121.20^{+22.34}_{-15.18}$	11:57:17	+49:16:58	25.39	39.5	17	1	Yes
NGC4942	$124.20^{+6.36}_{-5.32}$	13:04:19	-07:38:58	37.29	137.3	28.5	1	No
PGC3853	$128.11^{+1.58}_{-2.38}$	01:05:04	-06:12:45	41.37	105.33	13.8	1	Yes
NGC0337	$144.98^{+4.65}_{-4.09}$	00:59:49	-07:34:44	43.74	118.4	20.7	1	Unclear
NGC6509	$152.66^{+11.63}_{-9.11}$	17:59:25	+06:17:11	41	280.8	28.2	1	Yes
PGC6667	$155.32^{+4.29}_{-3.90}$	01:49:10	-10:03:40	33.96	122.87	24.6	1	No
NGC5964	$167.98^{+17.85}_{-14.07}$	15:37:36	+05:58:27	31.86	136.7	24.7	1	Yes
IC1291	$188.53^{+17.01}_{-13.68}$	18:33:52	+49:16:40	28	131.4	31.5	1	Yes
ESO555-G027	$188.74^{+42.05}_{-27.68}$	06:03:36	-20:39:04	20.87	221.5	24.3	1	Yes

Note. — Properties of all galaxies in this study. Columns are: (1) name of galaxy; (2) circular velocity determined from VLA data; (3 and 4) RA and DEC of center from ellipse task; (5) inclination derived from ellipse task axis ratio; (6) position angle from ellipse task; (7) distance; (8) reference for distance; (9) bar classification from visually examining CH1 data. References are 1: Catalog of Nearby Galaxies (Tully & Fisher 1988); 2: The Mark III Catalog of Galaxy Peculiar Velocities (Willick et al. 1997).

Table 2. GALFIT Results and PAH Flux

Galaxy (1)	Stage 1 (2)	Stage 2 (3)	Stage 3 (4)	Best Model (5)	PAH Flux (6)
ESO501-G023	Sérsic Profile $\chi^2_\nu = 1.779$ $r_e = 6.06$ $n = 2.02$	-	-	Stage 1	1.8 ± 0.1
UGC1862	Sérsic Profile $\chi^2_\nu = 2.034$ $r_e = 2.17$ $n = 0.63$	Sérsic Profile + PSF $\chi^2_\nu = 1.956$ $r_e = 2.00$ $n = 0.54$	-	Stage 2	5.4 ± 0.1
NGC4561	Sérsic Profile $\chi^2_\nu = 2.890$ $r_e = 1.35$ $n = 1.25$	Exponential Profile + Bar $\chi^2_\nu = 2.306$ $r_{s,disk} = 0.81$; $r_{e,bar} = 0.62$ $n_{disk} = 1$; $n_{bar} = 0.20$	-	Stage 2	9.6 ± 0.1
NGC3906	Sérsic Profile $\chi^2_\nu = 3.841$ $r_e = 1.92$ $n = 1.17$	Exponential Profile + Bar $\chi^2_\nu = 2.289$ $r_{s,disk} = 1.32$; $r_{e,bar} = 0.97$ $n_{disk} = 1$; $n_{bar} = 0.71$	-	Stage 2	9.0 ± 0.6
ESO418-G008	Sérsic Profile $\chi^2_\nu = 8.822$ $r_e = 2.01$ $n = 0.92$	Exponential Profile + Bar $\chi^2_\nu = 7.720$ $r_{s,disk} = 1.50$; $r_{e,bar} = 1.17$ $n_{disk} = 1$; $n_{bar} = 0.59$	-	Stage 2	8.1 ± 0.1
UGC6446	Sérsic Profile $\chi^2_\nu = 1.121$ $r_e = 44.86$ $n = 3.96$	-	-	Stage 1	0.5 ± 0.1
NGC2805	Sérsic Profile $\chi^2_\nu = 1.257$ $r_e = 20.40$ $n = 3.61$	Exponential Profile + PSF $\chi^2_\nu = 1.806$ $r_{s,disk} = 3.80$ $n_{disk} = 1$	Exponential Profile + PSF + Bulge $\chi^2_\nu = 1.179$ $r_{s,disk} = 6.89$; $r_{e,bulge} = 2.31$ $n_{disk} = 1$; $n_{bulge} = 1.42$	Stage 3	18.6 ± 0.1
ESO544-G030	Sérsic Profile $\chi^2_\nu = 2.174$ $r_e = 1.94$ $n = 0.64$	Sérsic Profile + PSF $\chi^2_\nu = 2.062$ $r_e = 1.96$ $n = 0.61$	-	Stage 1	7.1 ± 0.1
NGC3794	Sérsic Profile $\chi^2_\nu = 3.081$ $r_e = 4.02$	-	-	Stage 1	8.6 ± 0.1

Table 2—Continued

Galaxy	Stage 1	Stage 2	Stage 3	Best Model	PAH Flux
(1)	(2)	(3)	(4)	(5)	(6)
	$n = 1.72$				
NGC4713	Sérsic Profile $\chi^2_\nu = 6.630$ $r_e = 2.49$ $n = 1.09$	Exponential Profile + Bar $\chi^2_\nu = 6.187$ $r_{s,disk} = 1.60$; $r_{e,bar} = 0.61$ $n_{disk} = 1$; $n_{bar} = 0.65$	-	Stage 2	38.6 ± 0.2
NGC4519	Sérsic Profile $\chi^2_\nu = 3.267$ $r_e = 6.91$ $n = 2.40$	Exponential Profile + Bar $\chi^2_\nu = 2.457$ $r_{s,disk} = 3.68$; $r_{e,bar} = 2.44$ $n_{disk} = 1$; $n_{bar} = 2.29$	-	Stage 2	50.1 ± 0.1
UGC6930	Sérsic Profile $\chi^2_\nu = 1.589$ $r_e = 5.93$ $n = 2.00$	Exponential Profile + Bar $\chi^2_\nu = 1.418$ $r_{s,disk} = 2.68$; $r_{e,bar} = 0.83$ $n_{disk} = 1$; $n_{bar} = 0.75$	-	Stage 2	7.8 ± 0.1
NGC4942	Sérsic Profile $\chi^2_\nu = 2.185$ $r_e = 3.14$ $n = 1.21$	Exponential Profile + PSF $\chi^2_\nu = 2.047$ $r_{s,disk} = 1.87$ $n = 1$	-	Stage 2	12.8 ± 0.1
PGC3853	Sérsic Profile $\chi^2_\nu = 0.580$ $r_e = 6.88$ $n = 2.08$	Exponential Profile + Bar $\chi^2_\nu = 0.459$ $r_{s,disk} = 3.38$; $r_{e,bar} = 1.52$ $n_{disk} = 1$; $n_{bar} = 1.32$	-	Stage 2	9.4 ± 0.2
NGC0337	Sérsic Profile $\chi^2_\nu = 18.153$ $r_e = 3.01$ $n = 1.06$	Exponential Profile + Bar $\chi^2_\nu = 13.81$ $r_{s,disk} = 1.97$; $r_{e,bar} = 1.70$ $n_{disk} = 1$; $n_{bar} = 1.28$	-	Stage 2	78.5 ± 0.2
NGC6509	Sérsic Profile $\chi^2_\nu = 8.990$ $r_e = 3.21$ $n = 1.19$	Exponential Profile + Bar $\chi^2_\nu = 6.602$ $r_{s,disk} = 3.66$; $r_{e,bar} = 0.87$ $n_{disk} = 1$; $n_{bar} = 0.58$	-	Stage 2	48.6 ± 0.1
PGC6667	Sérsic Profile $\chi^2_\nu = 2.054$ $r_e = 4.55$ $n = 1.61$	Exponential Profile + Bar $\chi^2_\nu = 1.780$ $r_{s,disk} = 2.73$; $r_{e,bar} = 1.78$ $n_{disk} = 1$; $n_{bar} = 1.66$	-	Stage 2	10.9 ± 0.2
NGC5964	Sérsic Profile	Exponential Profile + Bar + PSF	-	Stage 2	9.6 ± 0.1

Table 2—Continued

Galaxy	Stage 1	Stage 2	Stage 3	Best Model	PAH Flux
(1)	(2)	(3)	(4)	(5)	(6)
	$\chi^2_\nu = 3.643$ $r_e = 17.46$ $n = 2.69$	$\chi^2_\nu = 2.125$ $r_{s,disk} = 5.98$; $r_{e,bar} = 2.91$ $n_{disk} = 1$; $n_{bar} = 0.76$			
IC1291	Sérsic Profile $\chi^2_\nu = 8.239$ $r_e = 5.43$ $n = 1.69$	Exponential Profile + Bar $\chi^2_\nu = 8.131$ $r_{s,disk} = 20.04$; $r_{e,bar} = 3.60$ $n_{disk} = 1$; $n_{bar} = 1.13$	-	Stage 2	10.9 ± 0.1
ESO555-G027	Sérsic Profile $\chi^2_\nu = 2.622$ $r_e = 4.34$ $n = 1.57$	Exponential Profile + Bar + PSF $\chi^2_\nu = 2.101$ $r_{s,disk} = 2.56$; $r_{e,bar} = 1.57$ $n_{disk} = 1$; $n_{bar} = 0.47$	-	Stage 2	11.9 ± 0.1

Note. — GALFIT output parameters and PAH fluxes in 21"-diameter circles centered at the galactic center. Columns are: (1) Name of galaxy; (2) Parameters for Stage 1 fit (Disk Model); (3) Parameters for State 2 fit (Disk + PSF and/or Bar); (4) Parameters for Stage 3 fit (Disk + Bar/PSF + Bulge); (5) Best fit for the galaxy; (6) PAH flux in mJy within a 21"-diameter circle centered on the galaxy. r_e is the effective radius, measured in kpc, such that half of the total flux is within r_e. r_s is the scalelength, measured in kpc, which is defined by $r_e = 1.678 r_s$. n is the Sérsic index from the Sérsic surface brightness profile.

REFERENCES

Allamandola, L. J., Tielens, A. G. G. M., & Barker, J. R. 1989, ApJS, 71, 733

Andredakis, Y. C., & Sanders, R. H. 1994, MNRAS, 267, 283

Bell, E. F. & de Jong, R. S. 2001, ApJ, 550, 212

Bertin, E. & Arnouts, S. 1996, AAPS, 317, 393

Böker, T. et al. 2002, AJ, 123, 1389

Böker, T. et al. 2004, AJ, 127, 105

Carollo, C. M. 1999, ApJ, 523, 566

Carollo, C. M. & Stiavelli, M. 1998, AJ, 115, 2306

Carollo, C. M., Stiavelli, M., de Zeeuw, P. T., & Mack, J. 1997, AJ, 114, 2366

Courteau S., de Jong, R. S., & Broeils, A. H. 1996, ApJ, 457, L73

Dalcanton, J. J., Yoachim, P., & Bernstein, R. A. 2004, ApJ, 608, 189

de Vaucouleurs G. 1948, AnAp, 11, 247

de Vaucouleurs G. 1963, ApJ, 8, 31

Eggen O.J., Lynden-Bell D., & Sandage A.R. 1962, ApJ, 136, 748

Erwin, P., & Sparke, L. S. 2002, AJ, 124, 65

Fathi, K., & Peletier, R.F. 2003, A&A, 407, 61

Fazio, G. G., et al. 2004, ApJS, 154, 10

Fisher, D. B. 2006, ApJ, 642, L17

Fisher, D. B. & Drory, N. 2008, AJ, 136, 773

Freeman, K. C. 1970, 160, 811

Graham, A. W., & Driver, S. P. 2005, PASA, 22, 118

Hasan, H. & Norman, C. 1990, ApJ, 265, 643

Häussler, B. et al. 2007, ApJS, 172, 615

Helou, G. et al. 2004, ApJS, 154, 253

Jedrzejewski, R. I., 1987, IAUS, 1217, 37

Kormendy, J. 1993, in IAU Symp. 153: Galactic Bulges, 209

Kormendy, J. & Kennicutt, R. C. 2004, ARA&A, 42, 603

Krist, J. & Hook, R. 1999, *TinyTim*

Nair, P. B. & Abraham, R. G. 2010, ApJ, 714, 260

Peng, C. Y., Ho, L. C., Impey, C. D., Rix, H. 2002, AJ, 124, 266

Regan, M. W. et al. 2006, ApJ, 652, 1112

Sandage A. 1990, JRASC, 84, 70

Schmidt M. 1959, ApJ, 129, 243

Seigar, M. S., Carollo, C. M., Stiavelli, M., de Zeeuw, P. T., & Dejognhe, H. 2002, AJ, 123, 184

Sérsic J. L. 1968, *Atlas de Galaxias Australes*. Córdoba: Obs. Astron. Univ. Nac. Córdoba

Toomre A. 1977a, *The Evolution of Galaxies and Stellar Populations*, ed. BM Tinsley, RB Larson, p. 401. New Haven: Yale University Observatory

Tully, R. B., & Fisher, J. R. 1988, *Catalog of Nearby Galaxies*, p. 224. Cambridge, UK: Cambridge University Press

Weinzirl, T. et al. 2009, ApJ, 696, 411

Willick et al. 1997, ApJS, 109, 333